

Modeling the Linear Polarization of GRB Afterglows Across the Electromagnetic Spectrum

Gal Birenbaum,^{1*} Omer Bromberg¹

¹*The Raymond and Beverly Sackler School of Physics and Astronomy, Tel Aviv University, Tel Aviv 69978, Israel*

Accepted XXX. Received YYY; in original form ZZZ

ABSTRACT

Linear polarization measurements in the optical band show polarization degrees of a few percents at late times. Recently, polarization at sub-percent level was also detected in radio by ALMA, opening the window for multi-wavelength polarimetry and stressing the importance of properly modeling polarization in GRB afterglows across the EM spectrum. We introduce a numerical tool that can calculate the polarization from relativistically moving surfaces by discretizing them to small patches of uniform magnetic field, calculating the polarized emission from each cell assuming synchrotron radiation and summing it to obtain the total degree of polarization. We apply this tool to afterglow shocks with random magnetic fields confined to the shock plane, considering electron radiative cooling. We analyze the observed polarization curves in several wavelengths above the cooling frequency and below the minimal synchrotron frequency and point to the characteristic differences between them. We present a method to constrain the jet opening angle and the viewing angle within the context of our model. Applying it to GRB 021004 we obtain angles of $\sim 10^\circ$ and $\sim 8^\circ$ respectively and conclude that a non-negligible component of radial magnetic field is required to explain the $\sim 1\%$ polarization level observed 3.5 days after the burst.

Key words: gamma-ray burst: general - polarization - methods: numerical

1 INTRODUCTION

A Gamma-Ray Burst (GRB) afterglow (AG) is formed when a relativistic jet plows through the interstellar medium (ISM) and gathers enough material ahead of it to considerably decelerate and dissipate its kinetic energy. The interaction of the jet with the ambient medium leads to the formation of two shocks: a forward shock, propagating into the ambient medium, which is responsible for most of the AG emission and a reverse shock, which grows in the ejecta and contributes to the emission at an early stage (e.g. Sari 1997; Kobayashi et al. 1999). The emission is well described by a broken power-law energy distribution of electrons gyrating around magnetic field lines and emitting synchrotron light (e.g. Paczynski & Rhoads 1993; Katz 1994; Katz & Piran 1997; Waxman 1997b,a; Sari et al. 1998; Mészáros et al. 1998). Though this model is very successful in describing the overall AG emission, detailed properties, such as the configuration of the magnetic field or the acceleration process of the non-thermal particles remain obscured. Such details can help us understand the properties of the ambient medium as well as of the relativistic jets. For example, a shock propagating into an unmagnetized medium can grow magnetic field in-situ via local plasma instabilities such as the two-stream Weibel instability (e.g. Medvedev & Loeb 1999; Medvedev et al. 2005). The

magnetic field in this case will be mostly tangential to the shock plane with a small coherence length. A radial component may grow downstream of the shock due to plasma motions. On the other hand the medium may contain a non-negligible ordered field component, as suggested by some models of ISM (e.g. Planck Collaboration et al. 2018) or in the case of a shock propagating in to a magnetized stellar wind (e.g. Biermann & Cassinelli 1993). In this case the shock compressed magnetic field can add a component with a large coherence length to the locally grown random field and alter the field configuration. In a case of a reverse shock, if relics of magnetic field from a magnetically launched jet remain in the upstream plasma, they will be imprinted on the shock and can alter both the particle acceleration process as well as the properties of the observed emission.

A natural way to probe the properties of magnetic fields in emitting systems is using polarization measurements. Synchrotron radiation from a distribution of particles is linearly polarized in a direction perpendicular to the magnetic field and to the line of sight (LOS). A detection of an overall polarization signature is indicative of a global anisotropy in the magnetic field or in the system geometry. A proper modeling of the polarization and how it evolves with time can shed light on the conditions in the emission regions, specifically on the configuration of the magnetic field in the shock and on the particle spectral energy distribution (SED).

So far linear polarization in the AG was observed in the opti-

* E-mail: galbirenbaum@mail.tau.ac.il

cal band. The first detections of polarization at a level of $\sim 1\%$ in the AGs of GRB 990510 (Covino et al. 1999a; Wijers et al. 1999) and GRB 990712 (Rol et al. 2000) inspired several analytic works that modeled the polarization assuming a random field configuration on the shock plane and synchrotron emitting electrons with a powerlaw SED (Covino et al. 1999b; Sari 1999b; Ghisellini & Lazzati 1999; Gruzinov & Waxman 1999). Later observations of GRB AGs with a higher polarization degree, e.g. GRB 020405 (Bersier et al. 2003; Covino et al. 2003), motivated models that calculated the polarization from a uniform magnetic field on the shock plane (Granot & Konigl 2003) and from a random field with a patchy geometrical pattern (Nakar & Oren 2004). Other detections of polarization showed rotations of the polarization vector over time (e.g. Rol et al. 2003; Wiersema et al. 2012) and changes in the polarization degree measured at different wavelengths (Klose et al. 2004). Lately, polarization at a sub-percentage level was also detected in mm wavelengths using ALMA (Laskar et al. 2019) opening a window for polarization modeling across a wide spectral range. This highlights the importance of modeling both the time evolution as well as the spectral properties of AG polarization.

When modeling the time evolution of the observed polarization, one needs to consider the differences in the light travel times from various regions on the shock (e.g. Sari 1998; Granot et al. 1999; Granot 2008). The effect on the observed polarization and its evolution in time was studied by many authors (e.g. Sari 1999a; Granot & Konigl 2003; Rossi et al. 2004; Gill et al. 2019). The spectral properties of the observed image were first calculated analytically by Sari (1999a) and by Granot et al. (1999) assuming a single powerlaw SED. Lately Shimoda & Toma (2020) used these results to obtain the time evolution of the polarization at frequency above and below the synchrotron frequency. These studies used analytic descriptions of the system and propagated them in time to obtain the polarization curves. We took a different approach of discretizing the emitting zone into individual cells, calculating the time dependent emission and polarization in each cell separately and summing the flux weighted polarization from all cells to obtain the total observed polarization. A similar approach was taken by Nava et al. (2015) in calculating the linear and circular polarization in spherical AG shocks with various magnetic field configurations, without accounting for photon travel time effects. This method allows us to plot detailed maps of the polarized images. In addition, it is highly flexible in varying the system properties, introducing asymmetries and adding more physical processes. Our method can work with arbitrary magnetic field configurations, viewing angles and particle SED. The current version calculates emission from 2D surfaces. We use it to calculate the polarization accounting for cooling of the emitting particles by using a broken power-law SED and obtain the observed polarization curves in the different spectral regimes.

We begin by describing the geometrical setup adopted in this work and the different reference frames we use (§2). We then discuss how we model the shock emission (§3) and the polarization (§4). In section 5 we present some indicative results and discuss their implications and differences from other works. Last, we present in §6 a method to obtain the observer’s viewing angle and the jet opening angle from two observables in the polarization curve. In this work we focus only on the forward shock, and assume a configuration of a random field tangent to the shock plane and a slow cooling SED. We leave the modeling of other configurations including the emission from reverse shocks to a future work.

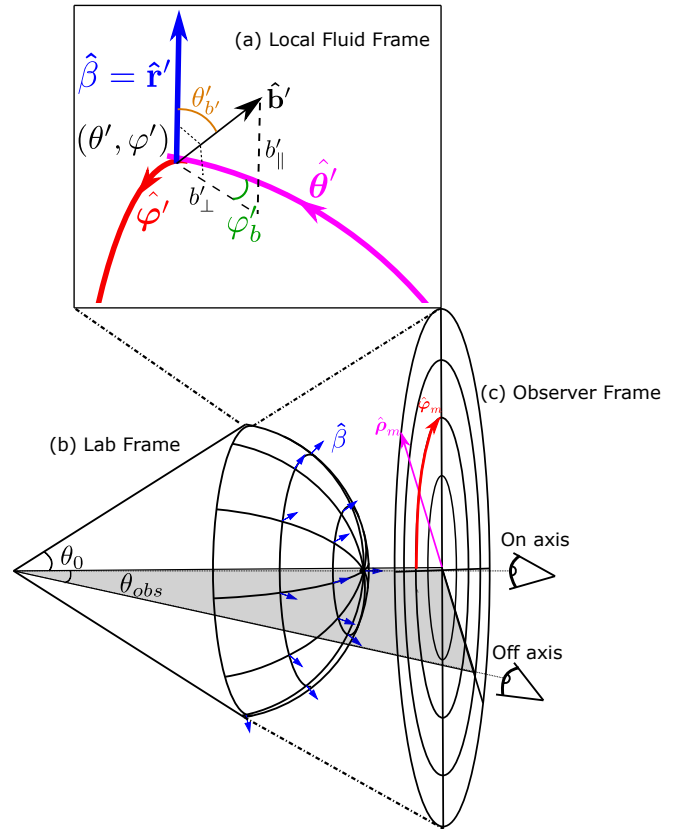


Figure 1. The setup of our system. The local fluid frame is shown in panel (a) with the magnetic field structure denoted by eq. 1. Panel (b) shows the AG shock in the lab frame. It has a semi-spherical shape with a half opening angle θ_0 . The shock symmetry axis is aligned with the \hat{z} axis. The matter at each point just behind the shock expands radially with a 3-velocity $\hat{\beta}$. Panel (c) shows the observer’s map. The image of the AG shock is projected on the map so that the coordinate θ on the AG shock is mapped into a radial distance on the map as $\rho_m = \sin \theta$ and the coordinate φ on the shock is mapped to the coordinate $\varphi_m = \varphi$. The observer is at rest with respect to the lab frame. On-axis observers are aligned with the shock symmetry axis, while an off-axis observer is rotated at an angle θ_{obs} from the symmetry axis.

2 GEOMETRICAL SETUP

Our system consists of a spherical-cap shaped blast-wave with a half opening angle θ_0 , propagating in a medium and driving a shock ahead of it. We assume that the observed emission comes from the fluid just behind the shock moving at a Lorentz factor $\Gamma = \Gamma_{sh}/\sqrt{2}$, where Γ_{sh} is the Lorentz factor of the shock¹. The symmetry axis is aligned with the \hat{z} axis, while the observer can be aligned with the jet axis (on-axis observer) or misaligned by an angle θ_{obs} from it (off-axis observer). We consider three inertial frames: i) The local fluid frame at the shock immediate downstream, located at the same radius as the shock. ii) The lab frame, in which the ambient medium is at rest. iii) The observer frame. We neglect cosmological expansion, thus the observer is at rest with respect to the lab frame. We use tagged values for quantities in the local fluid frame,

¹ In practice the emission comes from a layer of thickness $\sim R/\Gamma^2$ having a spread of Lorentz factors (see e.g. Piran et al. 1993), however since our model is 2D we assume that all the emission comes from an infinitely thin surface that coincides with the shock surface.

untagged values for lab frame quantities and sub index "obs" to mark quantities in the observer frame.

2.1 Local fluid frame geometry

The magnetic field in the local frame, \mathbf{b}' , is defined with the following two angles:

(i) $\theta'_b \in [0, \frac{\pi}{2}]$ determines the angle of \mathbf{b}' from the local radial direction. So that $b'_\perp \equiv b' \sin \theta'_b$ is the magnetic field component on the shock surface.

(ii) $\varphi'_b \in [0, 2\pi]$ measures the orientation of \mathbf{b}'_\perp in the azimuthal direction ($\hat{\phi}'$) from the local $\hat{\theta}'$ direction, namely $\cos \varphi'_b = \mathbf{b}'_\perp \cdot \hat{\theta}'$. The two angles are illustrated in fig. 1a.

With these definitions, a unit vector of the magnetic field in the local frame is defined as

$$\hat{\mathbf{b}}' = \cos \theta'_b \hat{\mathbf{r}}' + \sin \theta'_b \cos(\varphi' + \varphi'_b) \hat{\theta}' + \sin \theta'_b \sin(\varphi' + \varphi'_b) \hat{\phi}' \quad (1)$$

The choice of θ'_b and φ'_b allows us to define arbitrary configurations for the magnetic field. In this work we consider a random magnetic field on the plane of the shock, thus we use $\theta'_b = \frac{\pi}{2}$ and and randomize φ'_b at each cell.

2.2 Observer coordinate system and alignment

The observer's map is modeled as a projection of the spherical shock on a plane perpendicular to the jet axis so that the projected angular size is preserved² (see fig. 1b,c for illustration). The projected image is a circle centered around the jet axis, with 2D polar coordinates: $\rho_m = \sin \theta$, $\varphi_m = \varphi$ with a differential surface area

$$dS_m = \rho_m d\rho_m d\varphi_m = \cos \theta \sin \theta d\theta d\varphi = d\Omega_\perp. \quad (2)$$

For an on-axis observer, the LOS points in the $\hat{\mathbf{z}}$ direction. For any coordinate (ρ_m, φ_m) on the observer's map, the unit vector at the corresponding location on the shock pointing at the observer is

$$\hat{\mathbf{n}}_{\text{obs}} = \cos \theta \hat{\mathbf{r}} - \sin \theta \hat{\theta}. \quad (3)$$

To change the observer's viewing angle, we apply a rotation matrix, $R(\Psi, \hat{\mathbf{k}})$, where $\hat{\mathbf{k}}$ is the axis of rotation, Ψ is the rotation angle and the rotation is done according to the right hand rule with respect to $\hat{\mathbf{k}}$. In this work, we assume that all rotations of the observer are done about the $\hat{\mathbf{y}}$ axis. Therefore, the unit vector of an off-axis observer is $\hat{\mathbf{n}}_{\text{obs}} = R(\theta_{\text{obs}}, \hat{\mathbf{y}})\hat{\mathbf{z}}$, where $\theta_{\text{obs}} \equiv q\theta_0$ and $0 \leq q \leq 1$. The explicit expression for $\hat{\mathbf{n}}_{\text{obs}}$ on the shock surface is therefore

$$\begin{aligned} \hat{\mathbf{n}}_{\text{obs}} = & (\sin \theta \cos \varphi \sin \theta_{\text{obs}} + \cos \theta \cos \theta_{\text{obs}}) \hat{\mathbf{r}} \\ & + (\cos \theta \cos \varphi \sin \theta_{\text{obs}} - \sin \theta \cos \theta_{\text{obs}}) \hat{\theta} \\ & - \sin \varphi \sin \theta_{\text{obs}} \hat{\phi}. \end{aligned} \quad (4)$$

It can be seen that for $\theta_{\text{obs}} = 0$ the expression is equal to eq. 3. The mapping as well as the location of the observer are illustrated in fig. 1 on panels b and c.

² This is not the image an observer sees, but a convenient way to map each angle on the shock to a unique location on the observer's plane to assess and illustrate its contribution to the total polarization

2.3 Transformations of the observer LOS to the local fluid frame

To calculate the direction to the LOS in the local frame, we rotate $\hat{\mathbf{n}}_{\text{obs}}$ by an angle

$$\xi = \cos^{-1} \left(\frac{\mu_{\text{obs}} - \beta}{1 - \beta \mu_{\text{obs}}} \right) - \cos^{-1}(\mu_{\text{obs}}), \quad (5)$$

about the axis

$$\hat{\xi} = \hat{\beta} \times \hat{\mathbf{n}}_{\text{obs}}, \quad (6)$$

where $\mu_{\text{obs}} = \hat{\beta} \cdot \hat{\mathbf{n}}_{\text{obs}}$ depends on both θ and φ in the general case of an off-axis observer. The rotation is done by applying the rotation matrix, $R(\xi, \hat{\xi})$, obtaining

$$\hat{\mathbf{n}}'_{\text{obs}} = R(\xi, \hat{\xi})R(\theta_{\text{obs}}, \hat{\mathbf{y}})\hat{\mathbf{z}}. \quad (7)$$

This expression is a generalization of the classic aberration of light for an arbitrary viewing angle. In the case of an on-axis observer ($\theta_{\text{obs}} = 0$), we get that $\mu_{\text{obs}} = \cos \theta$ and the rotational angle is just

$$\xi = \theta' - \theta. \quad (8)$$

The rotation in this case is done along meridian lines about the $\hat{\xi} = -\hat{\phi}$ axis. The transformation from the shock frame back to the lab frame is done by rotating the LOS in the opposite direction, $(\hat{\mathbf{n}}'_{\text{obs}} \times \hat{\beta})$ and expressing ξ in terms of $\beta \cdot \hat{\mathbf{n}}'_{\text{obs}}$

3 EMISSION

The emission is calculated in the local fluid frame and boosted to the observer frame. Following the calculation of Sari et al. (1998) we consider a relativistic forward shock decelerating self-similarly in a medium with a uniform density (the ISM), according to the Blandford & McKee solution (Blandford & McKee 1976). Electrons are accelerated on the shock front to a power-law distribution in energy and emit synchrotron radiation in the presence of magnetic fields generated on the shock. The magnetic field in the local frame is parameterized as:

$$\mathbf{b}' = (32\pi\epsilon_b n m_p)^{\frac{1}{2}} \Gamma c \hat{\mathbf{b}}', \quad (9)$$

where m_p, n are the proton mass and number density in the ambient medium respectively and ϵ_b is the fraction of shock energy that goes to the magnetic field. The synchrotron power per unit frequency of a single electron is given by (Rybicki & Lightman 1979)

$$\dot{E}'_{e, \nu'}(\gamma) = \frac{\sqrt{3}e^3 b' \sin \alpha'}{m_e c^2} \bar{F} \left(\frac{\nu'}{\nu'_s(\gamma)} \right), \quad (10)$$

where $\bar{F}(x) = x \int_x^\infty K_{\frac{5}{3}}(\xi) d\xi$, is the integrated modified Bessel function of order $\frac{5}{3}$,

$$\nu'_s(\gamma) = \frac{3\gamma^2 e b' \sin \alpha'}{4\pi m_e c} \quad (11)$$

is the synchrotron frequency expressed with γ , the electron Lorentz factor in the shock frame and $\alpha' = \cos^{-1}(\hat{\mathbf{b}}' \cdot \hat{\mathbf{n}}'_{\text{obs}})$ is the pitch angle of the electrons radiating into the LOS. Note that although γ is defined in the local frame we leave it untagged. For the electron distribution we use the standard fast-cooling and slow-cooling distributions (Sari et al. 1998). The electron number density is assumed to be uniform in the flow. It has a broken powerlaw distribution in γ between a minimal Lorentz factor $\gamma_m \propto \Gamma$ and a maximal

value γ_{\max} with a break at γ_c , above which electrons cool over dynamical timescales and the particle distribution steepens. The fast-cooling distribution is relevant for early times. It is characterized by $\gamma_c < \gamma_m < \gamma_{\max}$ and has an electron number density distribution of

$$n'_\gamma \propto \begin{cases} \gamma^{-2} & \gamma_c < \gamma < \gamma_m \\ \gamma_m^{p-1} \gamma^{-p-1} & \gamma_m < \gamma < \gamma_{\max} \end{cases}. \quad (12)$$

Slow-cooling occurs at later times, is characterized by $\gamma_m < \gamma_c < \gamma_{\max}$ and has an electron number density distribution of

$$n'_\gamma \propto \begin{cases} \gamma^{-p} & \gamma_m < \gamma < \gamma_c \\ \gamma_c \gamma^{-p-1} & \gamma_c < \gamma < \gamma_{\max} \end{cases}. \quad (13)$$

The total emitted power per unit frequency is calculated by integrating the power per unit frequency of a single electron (eq. 10) over the entire electron population in the shock,

$$\dot{E}'_{\nu'} = \int \dot{E}'_{e,\nu'}(\gamma) N_\gamma d\gamma, \quad (14)$$

where $N_\gamma = C n'_\gamma$ is the total number of electrons per unit γ . The normalization coefficient C can be obtained by noting that the total number of radiating electrons is equal to the total number of electrons swept up by the shock, i.e. $C \int n'_\gamma d\gamma = \frac{2\pi(1-\cos\theta_0)}{3} R^3 n$. Assuming an isotropic distribution of magnetic field on the shock plane and of electron velocity we get that the specific intensity is $I'_{\nu'} = \dot{E}'_{\nu'}/2\pi(1-\cos\theta_0)R^2$. Transforming to the observer frame and noting that $I_\nu = D^3 I'_{\nu'/D}$ we get:

$$I_\nu = D^3 \frac{Rn}{3} \frac{\int \dot{E}'_{e,\nu'/D}(\gamma) n'_\gamma d\gamma}{\int n'_\gamma d\gamma} \propto D^{3-\kappa} R (b' \sin\alpha')^{1-\kappa} \gamma_m^{-2\kappa}, \quad (15)$$

where $D = [\Gamma(1-\beta\mu_{\text{obs}})]^{-1}$ is the Doppler factor of the shocked fluid and κ is the spectral slope at frequency ν/D . To integrate the spectral energy density in the numerator we use analytic approximations that hold both far and close to the critical frequencies $\nu'_{m,c} \equiv \nu'_s(\gamma_{m,c})$, as illustrated in fig. 2. This is opposed to the piecewise solution used in many analytic models (e.g. Sari et al. 1998). The difference between the two solutions becomes important when calculating the polarization spectrum as we show in sec. 4.1.

The observer's map in our model is an angular projection of the emitting surface on the sky. In order to evaluate the observed image in each map cell we need to calculate the specific flux per unit angle on the plane of the sky (surface brightness) that falls on each cell, defined as (e.g. Sari 1998)

$$\frac{dF_\nu(\rho_m, \varphi_m)}{dA} = I_\nu \left(\frac{R}{d_\perp} \right)^2 \mu_{\text{obs}} \frac{d^2_\perp}{R_\perp} \frac{d\mu_{\text{obs}}}{dR_\perp}, \quad (16)$$

where $R_\perp = R\sqrt{1-\mu_{\text{obs}}^2}$ is the perpendicular distance of the emitting element from the LOS and $dA = \frac{R_\perp dR_\perp d\varphi}{d_\perp^2}$ is a differential solid angle on the plane of the sky at the emission point. The LHS of eq. 16 is evaluated at the map coordinate (ρ_m, φ_m) , while the RHS is calculated at the corresponding shock coordinates (R, θ, φ) . The value of $\frac{d\mu_{\text{obs}}}{dR_\perp}$ is determined by the shape of the emitting surface (see below). The total flux on the map is obtained by integrating the differential flux

$$dF_\nu(\rho_m, \varphi_m) = \frac{dF_\nu}{dA} dA = I_\nu \left(\frac{R}{d_\perp} \right)^2 \mu_{\text{obs}} d\Omega \simeq I_\nu \left(\frac{R}{d_\perp} \right)^2 dS_m, \quad (17)$$

over all cells in the map. Note that when the observer is located at

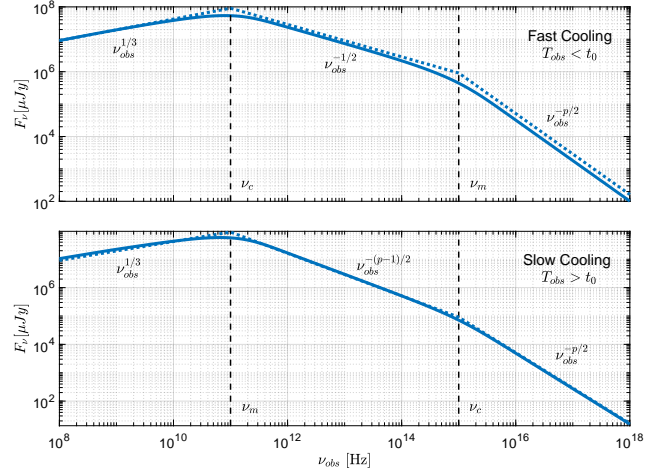


Figure 2. Spectral flux from a powerlaw distribution of electrons with a powerlaw index of $p = 2.5$ in two scenarios: i) Top panel: Fast cooling scenario, with $\nu_c < \nu_m < \nu_{\max}$. ii) Bottom panel: Slow cooling scenario, with $\nu_m < \nu_c < \nu_{\max}$. The locations of the critical frequencies ν_m, ν_c are marked with black vertical dashed lines. The solid blue lines show our smooth model while the dotted blue lines are the piecewise synchrotron spectrum used by Sari et al. (1998). The analytic spectrum is multiplied by 8 to match the numerical one. The origin of the factor 8 difference is discussed in appendix B.

an angle θ_{obs} from the jet axis, the map in our model is slightly misaligned with the LOS and the flux needs to be multiplied by an additional $\cos\theta_{\text{obs}}$. However since in this work $\theta_{\text{obs}} \leq \theta_0 \ll 1$ the effect is negligible and we ignore it.

3.1 Photon arrival times

Due to the relativistic motion, two photons emitted from the same point on the shock at a time difference δt in the lab frame reach the observer in a time interval

$$\delta T_{\text{obs}} = \delta t(1 - \beta_{\text{sh}}\mu_{\text{obs}}) \quad (18)$$

The difference between the emission time interval and the observed one leads to a mixing of photons emitted over a range of lab times and arrive to the observer simultaneously. This modifies the observed shape of the emitting surface from spherical to an egg-like shape denoted as the equal arrival time surface (EATS).

We define t as the time measured in the lab frame from the onset of the GRB and T_{obs} as the time in the observer frame that passed from the arrival of the first photon emitted at $t = 0$. To calculate the shape of the EATS we integrate eq. 18 and find the relation between T_{obs} and t for a case of a decelerating shock. We assume that the shock decelerates adiabatically, where the shock radius scales with its Lorentz factor as $R \propto \Gamma_{\text{sh}}^{-3/2}$ (e.g. Sari 1997). Expanding β_{sh} and μ_{obs} to first order, taking $R = ct$ and expressing the solution in terms of $\Gamma = \Gamma_{\text{sh}}/\sqrt{2}$, the shocked fluid Lorentz factor, the integration of eq. 18 gives (Sari 1998; Granot et al. 1999):

$$T_{\text{obs}} = t \left(1 - \mu_{\text{obs}} + \frac{1}{16\Gamma^2} \right). \quad (19)$$

and the associated radius is

$$R(T_{\text{obs}}, \mu_{\text{obs}}) = \frac{cT_{\text{obs}}}{1 - \mu_{\text{obs}} + \frac{1}{16\Gamma^2}}. \quad (20)$$

The shape of the EATS is obtained by fixing T_{obs} and calculating

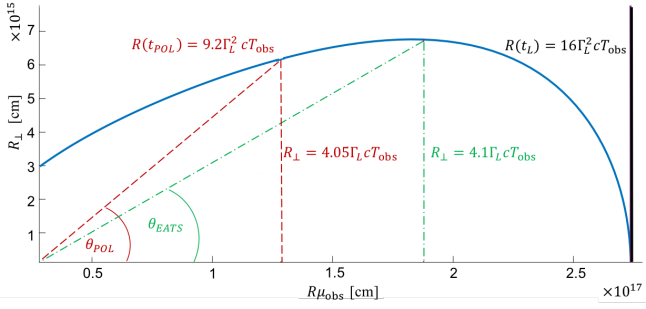


Figure 3. The shape of the EATS (blue), obtained from eq. 20, plotted on a plane perpendicular to the LOS at time $T_{\text{obs}} = 0.0602$ days. Radiation is emitted from each point on the EATS at a different lab time and reaches the observer at a time T_{obs} . The black vertical line is the shock surface at the lab time associated with T_{obs} on the LOS and $R(t_L) = 16\Gamma_L^2 c T_{\text{obs}}$ is its radius. The EATS maximum is located at a height $R_{\perp} \simeq 4.1\Gamma_L c T_{\text{obs}}$ (green dash-dotted line), and forms an opening angle of $\theta_{\text{EATS}} \simeq 0.4/\Gamma_L$ from the LOS. It divides the EATS to a front part and a back part located on the right and on the left of this point respectively. A second important angle, $\theta_{\text{POL}} \simeq 0.45/\Gamma_L$ (crimson dashed line), is the angle on the EATS for which the observed polarization is completely radial.

$R(T_{\text{obs}}, \mu_{\text{obs}})$. To connect the shock radius with the fluid Lorentz factor we calculate their value on the LOS, using the velocity profiles obtained from the Blandford-McKee solution and assuming that the total energy E in the flow is conserved (Sari et al. 1998):

$$R_L(T_{\text{obs}}) = \left(\frac{17ET_{\text{obs}}}{\pi m_p n c} \right)^{\frac{1}{4}}, \quad (21)$$

$$\Gamma_L(T_{\text{obs}}) = \frac{1}{4} \left(\frac{17E}{\pi n m_p c^5 T_{\text{obs}}^3} \right)^{\frac{1}{8}}. \quad (22)$$

With these quantities R and Γ maintain

$$\Gamma = \Gamma_L \left(\frac{R_L}{R} \right)^{\frac{3}{2}}. \quad (23)$$

An analytic solution to $R(T_{\text{obs}}, \mu_{\text{obs}})$ was given by Sari (1998); Granot et al. (1999) for an on-axis observer. Figure 3 shows the shape of the EATS on the $r - \theta$ plane calculated from eqn. 21-23 at time $T_{\text{obs}} = 0.0602$ days (see model parameters in sec. 5). It is consistent with the shapes obtained in previous works.

To calculate the observed surface brightness we need to calculate the quantity $\frac{1}{R_{\perp}} \frac{d\mu_{\text{obs}}}{dR_{\perp}}$ on the EATS. Using the above relations we obtain (see appendix A for the derivation)

$$\frac{1}{R_{\perp}} \frac{d\mu_{\text{obs}}}{dR_{\perp}} = \frac{1}{R^2} \left(\frac{1 + 3 \left(\frac{R}{R_L} \right)^4}{1 - 5 \left(\frac{R}{R_L} \right)^4} \right). \quad (24)$$

Substituting that in eq. 16 and calculating the corresponding $R(T_{\text{obs}}, \mu_{\text{obs}})$ and $\Gamma(T_{\text{obs}}, \mu_{\text{obs}})$ according to eqn. 21-23, we get the observed surface brightness at each cell on the map,

$$\frac{dF_{\nu}(\rho_m, \varphi_m)}{dA} = I_{\nu} \left(\frac{1 + 3 \left(\frac{R}{R_L} \right)^4}{1 - 5 \left(\frac{R}{R_L} \right)^4} \right) \mu_{\text{obs}}, \quad (25)$$

where I_{ν} is given in eq. 15. In appendix B we show a comparison of $\frac{dF_{\nu}(\rho_m, \varphi_m)}{dA}$ to the analytic expression obtained in (Sari 1998).

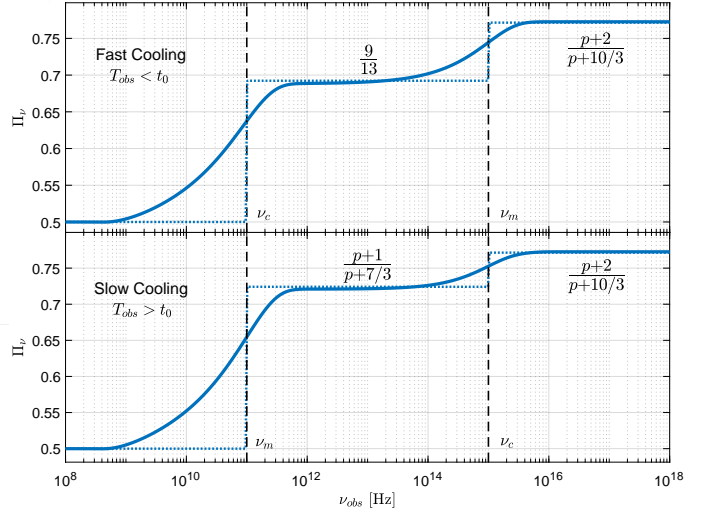


Figure 4. Polarization spectrum for a powerlaw distribution of electrons with a powerlaw index of $p = 2.5$ in two scenarios. i) Top panel: Fast cooling scenario, with $\nu_c < \nu_m < \nu_{\text{max}}$. ii) Bottom panel: Slow cooling scenario, with $\nu_m < \nu_c < \nu_{\text{max}}$. The locations of the critical frequencies ν_m, ν_c are marked with black vertical dashed lines. Solid blue lines depicts our semi-numeric solution, while the analytic step-function approximation is shown in dotted blue lines.

4 POLARIZATION

4.1 Polarization spectrum in a uniform field

While synchrotron radiation from a single particle is elliptically polarized, emission from a group of particles with a smooth pitch angle distribution is linearly polarized. For a group of particles with a distribution of Lorentz factors gyrating around a uniform magnetic field, the polarization degree can be expressed as (Rybicki & Lightman 1979).

$$\Pi_{\nu} = \frac{\int \tilde{G} \left(\frac{\nu}{\nu_s} \right) d n_{\gamma}}{\int \tilde{F} \left(\frac{\nu}{\nu_s} \right) d n_{\gamma}}, \quad (26)$$

where $\tilde{G}(x) = x K_{\frac{2}{3}}(x)$. In case of a powerlaw distribution of particles, $n(\gamma) \propto \gamma^{-p}$, the polarization degree can be approximated as $\Pi = \frac{p+1}{p+7/3}$ far from the distribution edges (Rybicki & Lightman 1979). Using this approximation, Granot (2003) fitted a polarization spectrum to the piecewise fast and slow cooling synchrotron spectra, obtaining step function solutions with jumps occurring at the various critical frequencies (fig. 4, dashed lines). We refined this calculation by evaluating Π over the smooth emission function we obtained in Section 3, using the same method for integrating the modified Bessel functions. Fig. 4 shows a comparison of our method to the analytic approximation of Granot (2003) for cases of fast cooling (upper panel) and slow cooling (low panel) synchrotron spectra. Our solution (solid lines) converges to the analytic model (dotted lines) far from the critical frequencies and changes gradually over a range of ~ 2 orders of magnitudes in frequencies close to them. A substantial difference from the analytic solution is seen at low frequencies, below $\nu_m(\nu_c)$ in the slow (fast) cooling spectrum. The difference can be important for measurements in the optical band at early times or at microwave-radio band at late times as we show below.

A change in the polarization degree can be seen if the polarization is measured instantaneously in several frequencies above and below a critical frequency (fig. 4). Alternatively, it can also be seen

when measuring the polarization in a single frequency over time, if during this time the observed frequency is crossed by a critical frequency. As the forward shock decelerates, the critical frequencies shift to lower values and may cross the observed frequency (Sari et al. 1998). We mark by $t_m(t_c)$ the time when $v_m(v_c)$ drops below the observed frequency. A third important time, marked by t_0 , occurs when v_c drops below v_m and the synchrotron spectrum shifts from fast cooling to slow cooling. Beyond this time the spectral slope for frequencies between v_m and v_c changes (see fig. 2) and the polarization degree changes accordingly.

4.2 The polarization vector in a general afterglow field

The polarization degree of light emitted by a single element with a uniform magnetic field is set by the spectral energy distribution of the emitting particles (fig. 4). In the general case, both the polarization vector and the polarization degree may vary between different emitting regions, altering the total polarization signature. To account for this effect we need to properly sum the contribution of polarized light from all regions. We calculate the direction of polarization in the local frame, transform it to the observer frame and sum the flux weighted contributions from all regions to obtain the total polarization. Our method follows the calculation of Nava et al. (2015) and generalizes it for arbitrary magnetic field configurations.

The direction of the polarization vector in each cell in the local frame is defined as

$$\hat{P}'_0 = \hat{n}'_{\text{obs}} \times \hat{b}', \quad (27)$$

where \hat{b}' is the unit vector of the magnetic field in a cell and \hat{n}'_{obs} is the direction to the observer in the local frame. For an on-axis observer, we can get an analytic expression to the local polarization angle in the observer frame. Taking the direction to the LOS in the local frame:

$$\hat{n}'_{\text{obs}} = \cos \theta' \hat{r}' - \sin \theta' \hat{\theta}' \quad (28)$$

together with the local frame magnetic field

$$\hat{b}' = \cos \theta'_b \hat{r}' + \sin \theta'_b \cos(\varphi' + \varphi'_b) \hat{\theta}' + \sin \theta'_b \sin(\varphi' + \varphi'_b) \hat{\phi}' \quad (29)$$

we get the direction of the polarization vector in the local frame,

$$\hat{P}'_0 = -[\sin \theta'_b \sin(\varphi' + \varphi'_b)] \hat{\psi}' + [\cos \theta' \sin \theta'_b \cos(\varphi' + \varphi'_b) + \sin \theta' \cos \theta'_b] \hat{\phi}', \quad (30)$$

where $\hat{\psi}' = \sin \theta' \hat{r}' + \cos \theta' \hat{\theta}'$ is a unit vector on the $\hat{r}' - \hat{\theta}'$ plane perpendicular to \hat{n}'_{obs} and to $\hat{\phi}'$. The polarization vector remains perpendicular to the LOS and to the magnetic field at any reference frame. Any rotation applied on \hat{n}'_{obs} (and \hat{b}') will rotate \hat{P}'_0 in the same way. The transformation of \hat{n}'_{obs} to the observer frame is obtained by applying the rotational matrix $R(\xi, \hat{\phi}')$, which rotates \hat{n}'_{obs} by an angle $\xi = \theta' - \theta$ about the $\hat{\phi}'$ axis (see sec. 2.3). The same rotation applied on \hat{P}'_0 rotates only the $\hat{\psi}'$ component by the same angle. Since $\hat{\psi}' \perp (\hat{n}'_{\text{obs}}, \hat{\phi}')$ it follows that $\hat{\psi} = R(\xi, \hat{\phi}') \hat{\psi}' \perp (\hat{n}_{\text{obs}}, \hat{\phi})$, and is in the direction of \hat{p}_m on the observer's map. We therefore get

$$\hat{P}_0 = -[\sin \theta'_b \sin(\varphi' + \varphi'_b)] \hat{p}_m + [\cos \theta' \sin \theta'_b \cos(\varphi' + \varphi'_b) + \sin \theta' \cos \theta'_b] \hat{\phi}_m. \quad (31)$$

The polarization angle in each map cell is denoted by $\frac{P_{\phi_m}}{P_{p_m}}$ and mea-

sured relative to the local ϕ_m :

$$\phi_{p_0} = \phi_m + \tan^{-1} \left[\frac{\sin \theta' \cot \theta'_b}{\sin(\varphi' + \varphi'_b)} + \cos \theta' \cot(\varphi' + \varphi'_b) \right]. \quad (32)$$

Transforming θ' to the lab frame results in

$$\phi_{p_0} \simeq \phi_m + \tan^{-1} \left[\frac{2y}{1+y^2} \frac{\cot \theta'_b}{\sin(\varphi' + \varphi'_b)} + \frac{1-y^2}{1+y^2} \cot(\varphi' + \varphi'_b) \right], \quad (33)$$

where $y = \Gamma\theta$. This expression extends the analytic expressions obtained by Nava et al. (2015) and by Granot & Konigl (2003) for a uniform magnetic field on the plane of the shock ($\theta'_b = \frac{\pi}{2}$, $\varphi'_b = 0$) and for a radial magnetic field ($\theta'_b = 0$) configurations. For an off-axis observer, ξ is calculated in a similar way as we show in eq. 5 and the rotation is done about the $(\hat{n}'_{\text{obs}} \times \hat{\beta})$ axis. The calculation of ϕ_{p_0} in this case is done numerically.

To calculate the total degree of polarization we construct the local Stokes parameters in each cell:

$$q_{v,0} = \Pi_v \cos 2\phi_{p_0}, \quad (34)$$

$$u_{v,0} = \Pi_v \sin 2\phi_{p_0}.$$

and weigh them by the surface brightness in the cell, divided by the total observed flux. The weighted q_v has the form

$$q_v = \frac{q_{v,0} \frac{dF_v}{dA}}{\int \frac{dF_v}{dA}}, \quad (35)$$

and is integrated to provide the total Q parameter:

$$Q_v = \int q_v dA = \frac{\int q_{v,0} \frac{dF_v}{dA} dA}{\int \frac{dF_v}{dA} dA}, \quad (36)$$

where $\frac{dF_v}{dA} dA$ is given in eq. 17. The parameter U is calculated in the same manner. From these we can obtain the global polarization degree, P_v and the position angle of the total polarization vector, $\theta_{v,p}$:

$$P_v = \sqrt{Q_v^2 + U_v^2} \quad (37)$$

$$\theta_{v,p} = \frac{1}{2} \tan^{-1} \left(\frac{U_v}{Q_v} \right).$$

Note that although the polarization angle in each cell is independent of frequency, the overall angle may depend on the observed frequency since the weight of each emitting region may depend on the frequency, as demonstrated in fig. 5.

5 RESULTS

We present results for polarization from a forward AG shock with a random magnetic field on the plane of the shock. We use the typical GRB parameters: $E_{\text{iso}} = 10^{52}$ ergs, $n = 1 \text{ cm}^{-3}$, $\theta_0 = 6^\circ$, $p = 2.5$, $\epsilon_e = 0.1$, $\epsilon_B = 0.01$ and take a distance of $d_L = 3.1 \cdot 10^{26}$ cm to the observer. In addition, the AG is modeled at times longer than t_0 , thus we only use the slow cooling spectrum. We run simulations with the observer located at different viewing angles from the jet axis, parametrized by $q = \frac{\theta_{\text{obs}}}{\theta_0}$. We present the observed polarization in three characteristic frequencies: 10^{18} Hz for the X-ray band, typically above the cooling frequency; 10^{15} Hz for the optical band, typically between v_c and v_m and 10^{11} Hz for the microwave band, typically below the synchrotron frequency.

The observed polarization depends on the local polarization degree and on the spatial distribution of the observed light on the map. To demonstrate the effect of the light distribution on the total polarization, we show in fig. 5 polarization maps in the optical (left) and microwave (right) bands seen by an observer aligned with the jet axis. The maps are 2D angular projection of a spherical-cap shock onto the observer plane, where the edge of the map corresponds to the jet opening angle, namely the maximal radial coordinate $\rho_{m,\max} = \sin \theta_0 \approx \theta_0$. The color scheme follows the observed intensity of light at each cell, and the short white lines mark the local direction of the polarization vector. All images are taken at the same T_{obs} . The top panels (panels a,c) show the surface brightness, $\frac{dF_v}{dA}$, the flux per unit of observed solid angle on the plane of the sky. This quantity represents the intensity seen by an observer at each map cell. The bottom panels show the flux per unit solid angle on the map, $\frac{dF_v}{dS_m}$, which represents the weight to the polarized light in each map cell. Since each cell on the map matches a unique angle on the emitting surface, regions with large weight contribute most to the total polarization.

Figure 5 panels (a,c): The surface brightness increases from the center, diverges at $\rho_m = \theta_{\text{EATS}}$ and drops to zero at $\rho_m > \theta_{\text{EATS}}$. The region with $\rho_m < \theta_{\text{EATS}}$ corresponds to the front of the EATS while $\rho_m > \theta_{\text{EATS}}$ shows the back of the EATS. (see fig. 3 for clarification). The surface brightness is the observed intensity scaled by a geometrical factor: the ratio of a differential solid angle on the emitting surface to its projection on the sky (eq. 25). The divergence of the surface brightness at θ_{EATS} occurs since the projected differential angle goes to zero and is a consequence of the 2D model. Another thing to notice is that the intensity of the microwave image is brighter than the optical at the center with respect to the peaks. The reason for that is the differences in the spectral slopes between the two bands. The observed intensity at cells with increasing ρ_m originates from regions on the EATS with higher Γ and thus decreasing ν' . Since $I'_{\nu'}$ has a positive (negative) slope in the microwave (optical) band, it becomes weaker (stronger) as ρ_m becomes larger. In the microwave band this effect counteracts the boost by the geometrical factor, leading to a more moderate increase in the surface brightness when moving from the center to the edge. As a result the center of the image appears brighter. The full calculation of the dependency of the surface brightness on ρ_m is shown in Appendix B.

Figure 5 panel b: Unlike the surface brightness, the differential flux density doesn't diverge at θ_{EATS} . In the optical image it forms a wide ring of high intensity at angles close to θ_{EATS} . The light coming from this ring is polarized mostly in the radial direction. To understand this, let's look at a circle with an opening angle $\theta_{\text{POL}} = 0.45/\Gamma_L = 1/\Gamma(\theta_{\text{POL}})$ from the LOS. (see fig. 3 for illustration and Appendix A for the derivation). This angle is translated to $\theta'_{\text{POL}} = \pi/2$ in the local emitting frame, namely the LOS is parallel to the shock surface and is aligned with the meridional direction ($\hat{\theta}'$). Suppose we take two orthogonal components of magnetic field in the local frame, an azimuthal component $b'_{\phi'}$ and a meridional one $b'_{\theta'}$ of equal values. Since $b'_{\theta'}$ points in the direction of the LOS in the local frame, only radiation can be observed. When transforming back to the observer frame, the polarization vector rotates and points in the $\hat{\rho}_m$ direction (see eq. 31). At the center of the map, the LOS is perpendicular to both $b'_{\phi'}$ and $b'_{\theta'}$. Therefore the polarization vector doesn't have a preferred direction. Since the center is much dimmer than the polarized ring, the majority of observed light in the optical band is polarized in the radial direction.

Figure 5 panel d: The differential flux density in the mi-

crowave band behaves differently than in the optical band. Instead of being limb brightened, most of the light is concentrated at the center of the image where the polarization is low. This effect originates from the scaling of I_v with ρ_m , which was explained qualitatively above. The scaling of the flux density can be quantified from eq. 15 by noting that

$$dF_v \propto R^2 I_v \propto D^{3-\kappa} R^3 \Gamma^{1-3\kappa} \propto D^{3-\kappa} \Gamma^{-(1+3\kappa)}, \quad (38)$$

where κ is the spectral slope at frequency ν and we ignore the contribution of $\sin \alpha'$ as it changes the result by a factor of order unity. Substituting the values of Γ and D at θ_{EATS} (see Appendix A for the exact values) and taking $\kappa = 1/3$, it can be shown that the differential flux at θ_{EATS} is half the flux on the LOS. For this reason the total observed polarization at frequencies below ν_m is typically lower than the polarization at frequencies above ν_m , as we show next.

An AG shock with a random magnetic field shows no net polarization when viewed on-axis, since the observed ring is symmetric about the LOS and the polarization cancels out. When the AG is observed off-axis, the observed ring is no longer centered around the symmetry axis. As the shock slows down, the visible area of the shock grows, causing the ring to expand. Eventually some parts of the ring grow beyond the shock edge and disappear before others. This breaks the symmetry and leads to a net polarization with distinct features (e.g. Sari 1999a; Ghisellini & Lazzati 1999; Granot & Konigl 2003). Figure 6 shows the evolution of an AG shock observed in the optical band at an angle $\theta_{\text{obs}} = 0.8\theta_0$ from the symmetry axis ($q = 0.8$). The middle panel shows the polarization curve and the bottom panel shows the evolution of the polarization vector position angle, measured from the vertical direction on the map. The dotted vertical lines mark four distinct episodes in the evolution of the polarization curve, titled a-d. The polarization maps associated with each episode are shown at the top panel. The center of the emission ring in each map is at $\rho_m = \theta_{\text{obs}}$ and is aligned with the LOS.

The total polarization in fig. 6 evolves as follows. As the forward shock decelerates, the ring expands and its right part disappears, creating a growing deficit in the amount of light with horizontal polarization, thus the total polarization in the vertical direction increases. The polarization degree reaches its first peak when the inner radius of the ring touches the edge of the map (*case a*). As the ring continues to grow an increasing amount of light with predominantly vertical polarization is removed and the total polarization decreases. When $\sim 1/2$ of the ring is outside the jet boundary, the vertically and horizontally polarized components balance each other and the net polarization zeros out (*case b*). From hereon, the dominant polarization component is horizontal and the total polarization position angle rotates by 90° . When the opening angle of the ring is $\sim (\theta_0 + \theta_{\text{obs}})$ the left side of the ring is at the edge of the jet, asymmetry reaches a maximum and the horizontal net polarization peaks (*case c*). At longer times the ring disappears and the observed light originate from the inner, exceedingly dimmer parts of the ring, resulting in a steepening of the AG lightcurve associated with a jet-break. This implies that the maximal polarization and the jet-break should occur at times close to each other. Since the polarization vector is more isotropically distributed in these parts, the net polarization drops (*case d*). In addition sideways expansion of the AG material, expected to occur after the jet-break (not simulated here), will lead to an even more symmetrical image and will reduce the total polarization degree even further (see e.g. Sari 1999a). Altogether the evolution shows two distinct peaks between which the polarization vector rotates by 90° and the polarization

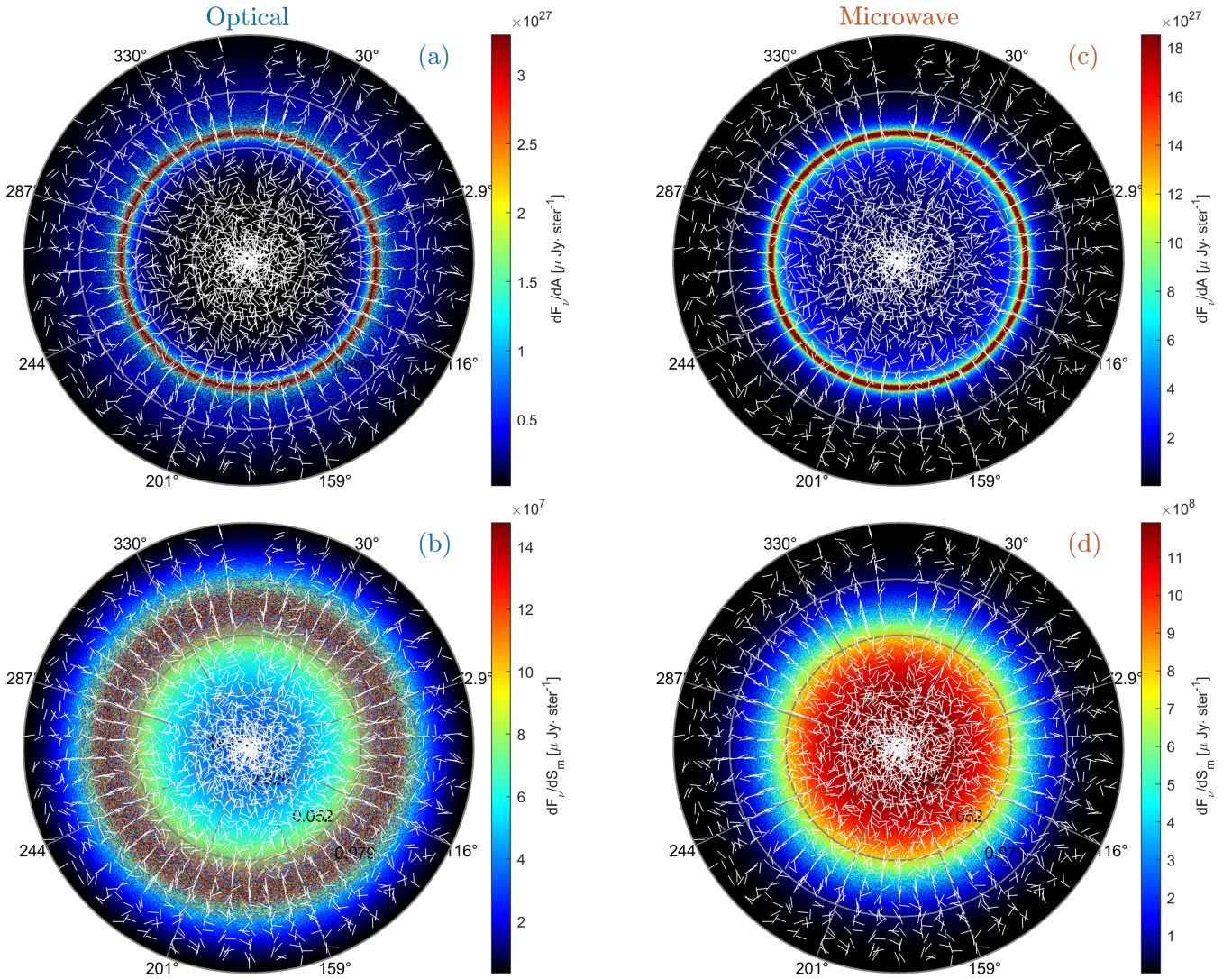


Figure 5. Intensity maps of an afterglow shock with the local polarization direction, projected on the observer’s plane (short white lines). All maps are shown at the same observer time. Left panels (a,b) show observed emission in the optical band ($v_{\text{obs}} > v_m$), and right panels (c,d) in the microwave band ($v_{\text{obs}} < v_m$). The top panels (a,c) show the surface brightness (flux per unit of solid angle on the plane of the sky). The surface brightness is dimmer at the center and diverges at the maximal opening angle of the EATS. The light at $\rho_m < \theta_{\text{EATS}}$ originates from the front of the EATS while the light at $\rho_m > \theta_{\text{EATS}}$ comes from the back of the EATS. The bottom panels show the flux per unit of surface on the map (corresponds to the flux per unit solid angle on the shock), which sets the scale of the polarized light at each point on the map. Here the observed image is different between the two bands. In the optical band most of the light is concentrated in a wide ring at opening angles close to θ_{EATS} , while in the microwave the emission is strongest at the center. The reason for that is the different spectral slopes at each band as we explain in the text. A steeper slope in the optical band also results in a higher sensitivity to the angle of the local magnetic field from the LOS ($\sin \alpha'$) leading to a more granular image. The polarization is mostly radial at ρ_m close to θ_{EATS} and it has no preferred direction along the LOS. When the AG is observed off-axis, the optical image will show higher net polarization than the microwave, as we show in fig. 7.

drops to zero. The occurrence time of these features and the height of the peaks depend on the observed frequency and on the viewing angle, as we show next.

Note that a rotation of the polarization vector is seen in the optical band also at early times, when the net polarization is close to zero. At these times the entire ring is visible and the polarization cancels out almost completely. The non zero value of the position angle is obtained due to residuals in the polarization and is set arbitrarily.

Apart from modifying the geometry of the observed image, the spectrum of the emitting particles also affects the polarization through the local polarization degree Π_V , as discussed in sec. 4.1. If the spectrum has a broken powerlaw shape, Π_V will have differ-

ent values depending on the value of v_{obs} relative to v_m and v_c (see fig. 4). Since v_m and v_c decrease with time as the shock decelerates, they may cross v_{obs} . This crossing changes the spectral slope at v_{obs} resulting in an increase in Π_V and correspondingly in P_V . Figure 7 demonstrates this effect by showing the polarization curves seen in each of the three fiducial frequencies in microwave (red), optical (blue) and X-ray (yellow) bands. The observer is located at an angle of $\theta_{\text{obs}} = 0.95\theta_0$ from the jet axis. Panel (a) shows the evolution of v_m and v_c in the observer frame along the LOS (dashed black lines). Panel (b) shows the evolution of Π_V in each band along the LOS (solid lines). For comparison, we show in dotted lines the values of Π_V based on the analytic spectral shape of a piecewise function [Granot \(2003\)](#). Panel (c) shows the evolution

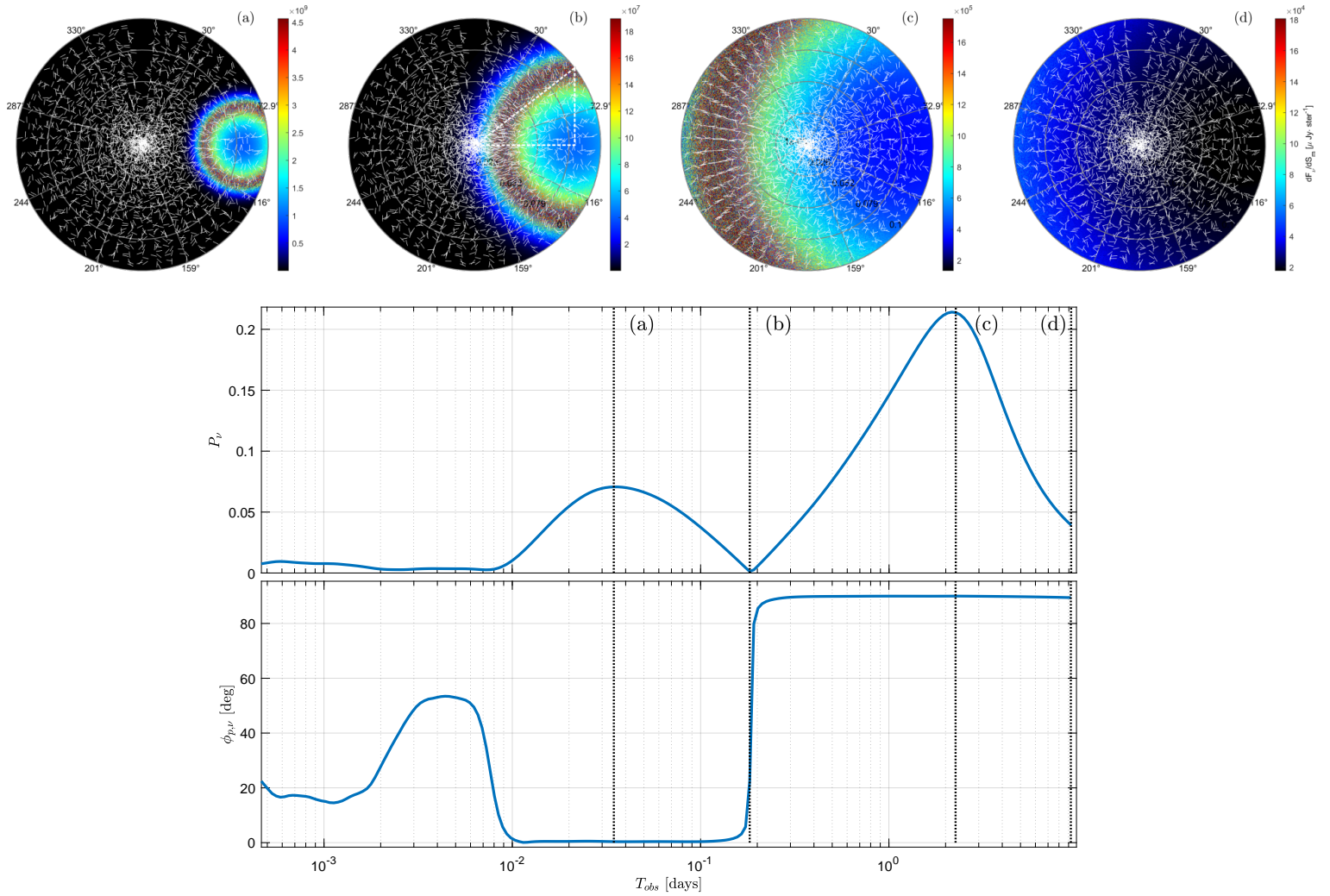


Figure 6. The time evolution of the total polarization in an AG shock observed at a frequency $\nu_{\text{obs}} = 10^{15}$ Hz from an angle $\theta_{\text{obs}} = 0.8\theta_0$. To focus on the geometrical effect alone, we set the local polarization degree $\Pi = 0.75$ in all cells. Top panel: The differential flux per unit observer map, $\frac{dF}{dS_{\text{obs}}}$, with the local polarization direction shown in white lines. Middle panel: Time evolution of the integrated polarization degree. Bottom panel: The projected angle of the polarization vector on the map, measured from the vertical direction. In case b, when $P_V = 0$ half of the emitting ring is visible. At this time the jet symmetry axis, the LOS and the point on the ring which touches the map edge form a right angle triangle, shown with dotted white line. the implications of that are discussed in section 6

of P_V , where the characteristic shape discussed above is seen in all three curves. Looking at panel (a), at early times both the X-ray and optical frequencies are crossed by a critical frequency. The crossing has a larger effect on Π_V in the optical band, increasing it by a factor of 1.5 over a decade in the time scale (from a few times 10^{-4} days to $\sim 5 \times 10^{-3}$ days). This changes the shape of the first bump, stretching it to later times in comparison to the bumps of the other frequencies (panel c). The peaks of the first bumps in the other wavelengths occur at roughly the same time. The ratio of the peak heights is directly related to the ratio of their Π_V values, which is about 1.5. At a later time ν_m crosses the microwave frequency. The corresponding rise in Π_V takes place throughout the entire duration of the second bump and pushes the peak of the bump to later times ($T_{\text{obs}} \sim 4$ days) as opposed to 2.5 days in the optical and X-ray bands. The differences in the peak polarization here are related to the alignment of the polarization vectors in the emitting rings. In the optical and X-ray bands the emission rings are polarized in the radial direction, while in the microwave band the polarization

vector is more isotropically oriented giving to a much lower overall polarization.

In figure 8 we show the polarization curves in the optical band measured by observers with different q values. The first peaks and zero polarization points occur at earlier times for larger q values. This is consistent with the fact that both times are related to part of the emitting ring that remains inside the observed image and therefore are connected with θ_{obs} , as shown in fig. 6. The stretching of the first bump of the $q = 0.95$ curve is a consequence of ν_m dropping below ν_{obs} at time t_m . The second peak occurs when the polarized ring is about to grow beyond the shock edge, which occurs when $(\theta_0 + \theta_{\text{obs}}) \gtrsim \theta_{\text{POL}} \simeq 0.45/\Gamma_L$. The condition gives a relation between q and the time of the second peak, where T_{obs} is roughly proportional to $(1+q)^{\frac{8}{3}}$, which explains the shift of the second peaks to later times at larger q values. The maximum polarization is connected with the asymmetry in the emission ring. As discussed above, the observed polarization at the time of the second peak is determined by the parts of the ring that remain in the observer's map (fig. 7c). At small q values the ring center is close

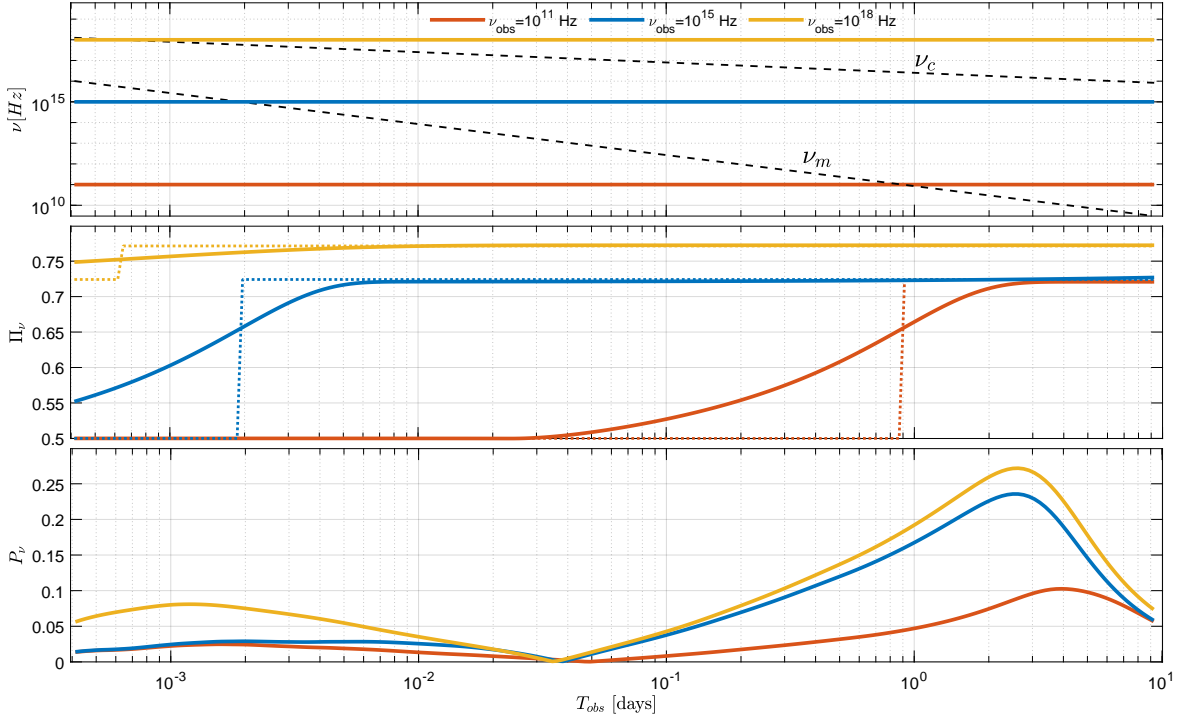


Figure 7. Polarization curves at the three simulated bands: microwave (red), optical (blue) and X-ray (yellow) seen by an observer at $\theta_{\text{obs}} = 0.95\theta_0$. Panel (a) shows the evolution of ν_c and ν_m on the LOS (dashed black lines) compared with the observing frequencies (solid colored lines). Panel (b) shows the local polarization degree, Π_v on the LOS. The solid and dotted lines show the value of Π_v according to our numerical calculations and according to the analytic estimation of Granot (2003) respectively. Panel (c) shows the polarization curves.

to the jet axis, and the ring image, which has a mean opening angle of $\sim \theta_0$ at that time, remains highly symmetric. As q increases the ring center moves closer to the map edge, the asymmetry in the observed image increases and as a result the polarization rises. The maximal values we obtain are consistent with other works (e.g. Rossi et al. 2004; Shimoda & Toma 2020).

6 IMPLICATIONS ON THE VIEWING ANGLE

So far almost all measurements of linear polarization at times longer than a few thousand seconds show P_v values smaller than $\sim 5\%$ (e.g. Covino et al. 2004). In those few GRBs where the time of the measured polarization coincides with a possible jet-break (Greiner et al. 2003; Wiersema et al. 2012, e.g.), the polarization can be used to place an upper limit on the observer’s viewing angle, since the jet-break occurs around the time of maximal polarization. Within our model the observed values imply $q \lesssim 0.2$.

If the magnetic field has a radial component as well, it will add an azimuthal polarization component that will reduce the total polarization and can account for higher values of q . In such a case there is an alternative way to constrain θ_{obs} by observing a zeroing of the polarization degree in coincidence with a rotation of the polarization angle by 90° . Such an event is indicative for a general configuration of random field with a uniform strength on the shock (e.g. Granot & Konigl 2003). The following is applicable for observations in the optical band. At the time of polarization zero, half of the emission ring is visible to the observer (see fig. 6b). At this time one can imagine a right-angle triangle between three points on the observer’s map: the jet symmetry axis, the LOS and the point where

the ring intersects with the map edge, which gives the relation

$$\theta_{\text{obs}}^2 + \theta_{\text{POL},1}^2 \simeq \theta_0^2. \quad (39)$$

If in addition a polarization peak is observed at a later time, or alternatively a jet-break is identified, one can get a second constraint on the system parameters,

$$\theta_0 + \theta_{\text{obs}} \simeq \theta_{\text{POL},2}, \quad (40)$$

where $\theta_{\text{POL},1}$ and $\theta_{\text{POL},2}$ are measured at the times of polarization zero and second polarization peak respectively. Note that we use θ_{POL} rather than θ_{EATS} here, since the flux and the alignment of the polarization vector are maximal on θ_{POL} , thus it has the largest impact on the polarization evolution. Substituting the relation between θ_{POL} and the Lorentz factor on the LOS, $\theta_{\text{POL}} = 0.45/\Gamma_L$ (see. appendix A), we get the expressions

$$\begin{aligned} \theta_0 &= \frac{0.45}{2\Gamma_{L,2}} \left(1 + \left(\frac{\Gamma_{L,2}}{\Gamma_{L,1}} \right)^2 \right) \\ \theta_{\text{obs}} &= \frac{0.45}{2\Gamma_{L,2}} \left(1 - \left(\frac{\Gamma_{L,2}}{\Gamma_{L,1}} \right)^2 \right), \end{aligned} \quad (41)$$

where $\Gamma_{L,1}$ and $\Gamma_{L,2}$ are the Lorentz factors associated with $\theta_{\text{POL},1}$ and $\theta_{\text{POL},2}$ respectively. Given an AG model, one can estimate $\Gamma_L(T_{\text{obs}})$ (e.g. with eq. 22) and obtain both θ_{obs} and θ_0 . These relations work well with our simulation data, reproducing both angles at an accuracy of $\sim 10\%$.

The flip in the direction of the polarization vector, alongside with the zeroing of P_v , occurs almost instantaneously and requires continuous monitoring of the AG to be detected. To date we know of a single such event that was observed in GRB 021004 ~ 0.4 days after the burst (Rol et al. 2003). The AG was monitored by

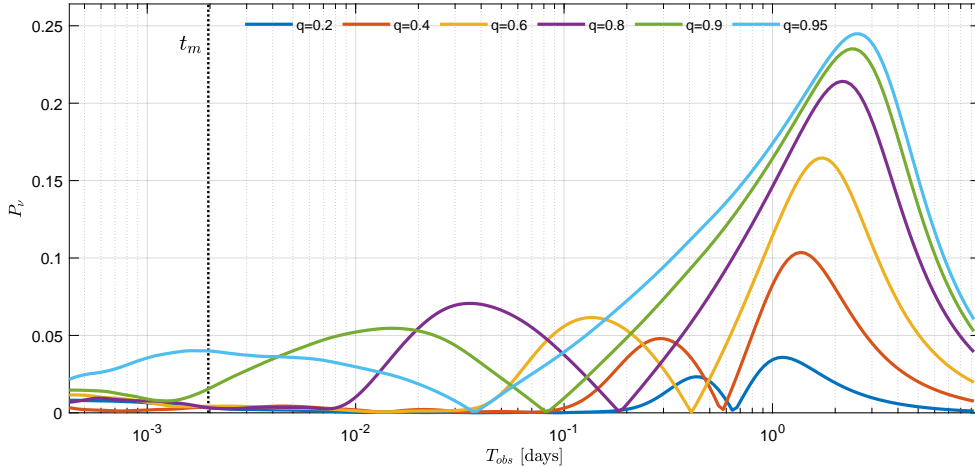


Figure 8. The time evolution of the integrated polarization degree at $\nu_{\text{obs}} = 10^{15}$ Hz, measured by an observer at various viewing angles from the LOS (parameterized by $q = \frac{\theta_{\text{obs}}}{\theta_0}$). The dotted vertical line marks the time when ν_m drops below ν_{obs} resulting in an increase in P_v and to the stretch of the first bump in the polarization curve of $q = 0.95$.

Holland et al. (2003) during the first month, who fitted it with $E_{\text{iso}} = (2.2 \pm 0.3) \times 10^{52}$ erg, $n_{\text{ISM}} \approx 35 \times 10^{-3} \text{ cm}^{-3}$ (assuming a uniform ambient density) and a jet-break time at 4.74 ± 0.14 days. Taking the jet break time as an indication for the polarization peak, calculating the associated Lorentz factors with eq. 22 and substituting them in eq. 41 we obtain $\theta_0 = 10.3 \pm 0.3^\circ$, $\theta_{\text{obs}} = 7.5 \pm 0.3^\circ$ and $q = 0.73 \pm 0.02^3$. Our estimate of θ_0 agrees with the one given by Holland et al. (2003). A relatively small polarization signature of $P_v \simeq 1\%$ measured at $T_{\text{obs}} = 3.5$ days, close to the jet-break (Rol et al. 2003), indicates that there should be radial magnetic field in addition to the component tangential to the shock plane with a comparable strength.

7 CONCLUSIONS

We present a computational method to calculate the observed polarization from relativistically moving surfaces by discretizing them, calculating the emission and polarization in each cell and summing up the flux weighted polarization from all cells to obtain the total polarization. Our method can work with arbitrary magnetic field configurations, system properties and observer viewing angles. It can also generate detailed polarization maps of the observed image that can help analyzing it. We apply the method on AG forward shocks propagating in a medium with a uniform density and carrying random magnetic fields on the plane of the shock. We study the time evolution of the polarization vector observed at different frequencies relative to the synchrotron critical frequencies and different viewing angles.

We reproduce analytic results for the shape of the surface from which photons arrive to the observer simultaneously (EATS) and for the observed emission. The polarization at each cell in the observer's map is scaled by the flux through the cell. For $\nu_{\text{obs}} > \nu_m$ most of the flux is concentrated in a wide ring at the edge of the EATS having an angle $\theta_{\text{EATS}} \simeq 0.4/\Gamma_L$ from the LOS (Sari 1998). The light coming from the ring is highly polarized in the radial direction, leading to a net polarization if the AG is observed off-axis and only part of the ring is revealed. In frequencies above ν_c , the

polarized ring is brighter due to the steeper spectral slope, leading to a higher polarization degree for the same conditions. At frequencies below ν_m the situation is reversed. The flux is more evenly distributed on the map with the point along the LOS being twice as bright as at θ_{EATS} , leading to a total polarization that is lower than in the previous cases.

We follow the time evolution of polarization in three frequencies where each frequency is associated with a different spectral regime in the slow cooling synchrotron spectrum. All polarization curves viewed with $0 < q < 1$ show three distinct features of two bumps and a point of zero polarization in between where the polarization vector rotates by 90° (e.g. Ghisellini & Lazzati 1999; Sari 1999a; Granot & Konigl 2003; Rossi et al. 2004). We show that in the optical band the first maximum occurs when the inner ring radius is touching the edge of the AG shock, and that the zero polarization occurs when half of the ring disappears. The second maximum occurs when the ring angular size is $\sim \theta_0 + \theta_{\text{obs}} = \theta_0(1+q) \simeq \theta_{\text{POL}}$, where the peak value increases with q . On θ_{POL} the polarization vector is completely radial and has a maximal weight, thus this angle has the largest influence on the observed polarization.

The spectral slope also controls the value of the local polarization degree, Π_v . To properly account for this effect we calculated the specific intensity and the Stocks parameters (eqn. 15, 36), carefully modelling the spectral shape close to the critical frequencies, instead of using the standard analytic piece-wise approximation. We obtained smooth solutions for Π_v , which allowed us to better quantify the changes in the polarization degree when ν_{obs} is crossed by a critical frequency. We demonstrate the effect on the polarization curves in the three fiducial frequencies and show that the crossing leads to a gradual increase in the total polarization P_v , which can occur over more than an order of magnitude in time relative to the onset of the transition. This can alter the shape of bumps in polarization curves by increasing the value of the peak and pushing it to later times.

Last, we introduced a method to estimate the jet opening angle and observing angle based on two distinct times, the time of zero polarization and the time of the second polarization peak, which occurs close to the jet-break time. We demonstrate the method on GRB 021004 and obtain a jet opening angle of $\theta_0 \simeq 10^\circ$, consistent with other estimations Holland et al. (e.g. 2003), and an observed angle of $\theta_{\text{obs}} \simeq 0.7\theta_0$. A polarization measurement of $P_v \sim 1\%$

³ The actual errors are likely larger due to systematics, mostly the time of the peak polarization relative to the jet-break time.

made at a time close to the jet-break time (Rol et al. 2003), points to the existence of a magnetic field with a radial component comparable to the component tangential to the shock. The conclusion agrees with the view that the magnetic field may develop a non negligible radial component downstream of the shock (e.g. Gill & Granot 2020). Since our model is 2D, the field we use is an average field from all emitting layers behind the shock. Additional detections of GRB AGs with large polarization angle rotations, accompanied by a zeroing of P_V , may help further constrain the observer viewing angle and the properties of magnetic field on the shock.

ACKNOWLEDGEMENTS

We thank Ehud Nakar, Jonathan Granot and Ore Gottlieb for helpful discussions. This research was supported by an ISF grant 1657/18 and by an ISF (Icore) grant 1829/12. The maps in this work were plotted using the polarPcolor tool by Cheynet (2020).

REFERENCES

- Bersier D., et al., 2003, *ApJ*, **583**, L63
 Biermann P. L., Cassinelli J. P., 1993, *A&A*, **277**, 691
 Blandford R. D., McKee C. F., 1976, *Physics of Fluids*, **19**, 1130
 Cheynet E., 2020, *ECheynet/polarPcolor* v3.8, doi:10.5281/ZENODO.3774156, <https://zenodo.org/record/3774156>
 Covino S., et al., 1999a, GRB Coordinates Network, **330**, 1
 Covino S., et al., 1999b, *A&A*, **348**, L1
 Covino S., et al., 2003, *A&A*, **400**, L9
 Covino S., Ghisellini G., Lazzati D., Malesani D., 2004, in Feroci M., Frontera F., Masetti N., Piro L., eds, *Astronomical Society of the Pacific Conference Series Vol. 312, Gamma-Ray Bursts in the Afterglow Era*, p. 169 ([arXiv:astro-ph/0301608](https://arxiv.org/abs/astro-ph/0301608))
 Ghisellini G., Lazzati D., 1999, *MNRAS*, **309**, L7
 Gill R., Granot J., 2020, *MNRAS*, **491**, 5815
 Gill R., Granot J., Kumar P., 2019, *MNRAS*, p. 2582
 Granot J., 2003, *The Astrophysical Journal*, **596**, L17
 Granot J., 2008, *MNRAS*, **390**, L46
 Granot J., Konigl A., 2003, *The Astrophysical Journal*, **594**, L83
 Granot J., Piran T., Sari R., 1999, *ApJ*, **513**, 679
 Greiner J., et al., 2003, *Nature*, **426**, 157
 Gruzinov A., Waxman E., 1999, *ApJ*, **511**, 852
 Holland S. T., et al., 2003, *AJ*, **125**, 2291
 Katz J. I., 1994, *ApJ*, **422**, 248
 Katz J. I., Piran T., 1997, *ApJ*, **490**, 772
 Klose S., Palazzi E., Masetti N., Stecklum B., Greiner J., Hartmann D. H., Schmid H. M., 2004, *A&A*, **420**, 899
 Kobayashi S., Piran T., Sari R., 1999, *ApJ*, **513**, 669
 Laskar T., et al., 2019, *ApJ*, **878**, L26
 Medvedev M. V., Loeb A., 1999, *ApJ*, **526**, 697
 Medvedev M. V., Fiore M., Fonseca R. A., Silva L. O., Mori W. B., 2005, *ApJ*, **618**, L75
 Mészáros P., Rees M. J., Wijers R. A. M. J., 1998, *ApJ*, **499**, 301
 Nakar E., Oren Y., 2004, *ApJ*, **602**, L97
 Nava L., Nakar E., Piran T., 2015, *MNRAS*, **1606**, 1594
 Paczynski B., Rhoads J. E., 1993, *ApJ*, **418**, L5
 Piran T., Shemi A., Narayan R., 1993, *MNRAS*, **263**, 861
 Planck Collaboration et al., 2018, *A&A*, **610**, C1
 Rol E., et al., 2000, *ApJ*, **544**, 707
 Rol E., et al., 2003, *A&A*, **405**, L23
 Rossi E. M., Lazzati D., Salmonson J. D., Ghisellini G., 2004, *MNRAS*, **354**, 86
 Rybicki G. B., Lightman A. P., 1979, *Radiative processes in astrophysics*. New York : Wiley, New York

- Sari R., 1997, *ApJ*, **489**, L37
 Sari R., 1998, *ApJ*, **494**, L49
 Sari R., 1999a, *The Astrophysical Journal*, **524**, L43
 Sari R., 1999b, *ApJ*, **524**, L43
 Sari R., Piran T., Narayan R., 1998, *ApJ*, **497**, L17
 Shimoda J., Toma K., 2020, arXiv e-prints, p. [arXiv:2005.03710](https://arxiv.org/abs/2005.03710)
 Waxman E., 1997a, *ApJ*, **485**, L5
 Waxman E., 1997b, *ApJ*, **489**, L33
 Wiersema K., et al., 2012, *MNRAS*, **426**, 2
 Wijers R. A. M. J., et al., 1999, *ApJ*, **523**, L33

APPENDIX A: THE EATS EQUATIONS

In order to obtain the EATS quantities used in this work we re-develop the EATS equations from (Sari 1998) and derive various quantities used in this work. We start with the equation for the radius of the EATS, eq. 20:

$$R(T_{\text{obs}}, \mu_{\text{obs}}) = \frac{cT_{\text{obs}}}{1 - \mu_{\text{obs}} + \frac{1}{16\Gamma^2}}, \quad (\text{A1})$$

where Γ is the Lorentz factor of the fluid just behind the shock. We can express it in terms of the Lorentz factor and EATS radius on the LOS through $\Gamma = \Gamma_L \left(\frac{R}{R_L} \right)^{-\frac{3}{2}}$, where $R_L = 16\Gamma_L^2 T_{\text{obs}}$. Substituting these in eq. A1 we get an equation for the observed EATS opening angle

$$1 - \mu_{\text{obs}} = \frac{1}{16\Gamma_L^2} \left(\frac{R_L}{R} - \left(\frac{R}{R_L} \right)^3 \right), \quad (\text{A2})$$

and from that we can obtain the perpendicular radius to the LOS at each point:

$$R_{\perp} = R \sqrt{1 - \mu_{\text{obs}}} = \frac{\sqrt{2}R_L}{4\Gamma_L} \sqrt{\frac{R}{R_L} - \left(\frac{R}{R_L} \right)^5}. \quad (\text{A3})$$

The surface brightness is defined as the specific flux per unit of solid angle on the sky,

$$\frac{dF_V(\rho_m, \varphi_m)}{dA} = I_V \left(\frac{R}{d_L} \right)^2 \mu_{\text{obs}} \frac{d_L^2}{R_{\perp}} \frac{d\mu_{\text{obs}}}{dR_{\perp}}, \quad (\text{A4})$$

where $dA = \frac{R_{\perp} dR_{\perp} d\varphi}{d_L^2}$ and d_L is the distance from the source. To calculate this quantity we need to evaluate $\frac{d\mu_{\text{obs}}}{dR_{\perp}} = \frac{d\mu_{\text{obs}}}{dR} \frac{dR}{dR_{\perp}}$. From eq. A2 we get that

$$\frac{d\mu_{\text{obs}}}{dR} = \frac{R_L}{16\Gamma_L^2 R^2} \left(1 + 3 \left(\frac{R}{R_L} \right)^4 \right), \quad (\text{A5})$$

and from eq. A3:

$$\frac{dR_{\perp}}{dR} = \frac{R_L}{16\Gamma_L^2 R_{\perp}} \left(1 - 5 \left(\frac{R}{R_L} \right)^4 \right) \quad (\text{A6})$$

resulting in:

$$\frac{1}{R_{\perp}} \frac{d\mu_{\text{obs}}}{dR_{\perp}} = \frac{1}{R^2} \frac{\left(1 + 3 \left(\frac{R}{R_L} \right)^4 \right)}{\left(1 - 5 \left(\frac{R}{R_L} \right)^4 \right)}. \quad (\text{A7})$$

Eq. A7 can be substituted in eq. A4 to obtain the surface brightness

$$\frac{dF_\nu(\rho_m, \phi_m)}{dA} = I_\nu \mu_{\text{obs}} \frac{\left(1 + 3 \left(\frac{R}{R_L}\right)^4\right)}{\left(1 - 5 \left(\frac{R}{R_L}\right)^4\right)}, \quad (\text{A8})$$

which is given in eq. 16. We further evaluate the opening angle of the EATS by equating $\frac{dR_L}{dR} = 0$ giving

$$R_{\text{EATS}} = R_L \left(\frac{1}{5}\right)^{\frac{1}{4}}, \quad (\text{A9})$$

and substituting that in eq. A3:

$$R_{\perp, \text{EATS}} = \frac{R_L}{\Gamma_L} \frac{1}{5^{\frac{1}{8}} \sqrt{10}} \quad (\text{A10})$$

The EATS opening angle is defined as $\theta_{\text{EATS}} \simeq \sin \theta_{\text{EATS}} = \frac{R_{\perp, \text{EATS}}}{R_{\text{EATS}}}$:

$$\theta_{\text{EATS}} \simeq \frac{5^{\frac{1}{8}}}{\sqrt{10}} \frac{1}{\Gamma_L} = \frac{1}{\sqrt{2} \Gamma_{\text{EATS}}}. \quad (\text{A11})$$

Both $R_{\perp, \text{EATS}}$ and θ_{EATS} are shown in fig. 20. Last, we derive the angle θ_{POL} on the EATS, for which $\Gamma_{\text{POL}} \theta_{\text{POL}} = 1$. At this angle the observed polarization is purely radial. For this we solve the equation

$$\frac{R_{\perp}}{R} \Gamma_L \left(\frac{R_L}{R}\right)^{\frac{3}{2}} = \frac{\sqrt{2}}{4} \left(\frac{R_L}{R}\right)^2 \sqrt{1 - \left(\frac{R}{R_L}\right)^4} = 1, \quad (\text{A12})$$

resulting in

$$R_{\text{POL}} = R_L \left(\frac{1}{9}\right)^{\frac{1}{4}} \quad (\text{A13})$$

$$R_{\perp, \text{POL}} = \frac{R_L}{\Gamma_L} \frac{1}{9^{\frac{1}{8}} \sqrt{9}},$$

and a corresponding opening angle

$$\theta_{\text{POL}} \simeq \frac{9^{\frac{1}{8}}}{\sqrt{9}} \frac{1}{\Gamma_L} = \frac{1}{\Gamma_{\text{POL}}}. \quad (\text{A14})$$

Note that θ_{POL} is slightly larger than θ_{EATS} and is located at the back part of the EATS.

APPENDIX B: COMPARISONS TO ANALYTIC RESULTS

We test the angular dependency of the surface brightness on the EATS, by comparing it to the analytic expressions in Sari (1998). An important difference between our method and the analytic calculation is how each method considers the effect of the pitch angle, α' , on the observed emission. The synchrotron power of an electron at an angle θ from the LOS depends on $(\sin \alpha')$, where $\alpha' = \cos^{-1}(\hat{b}' \cdot \hat{\theta}')$. Analytic methods have a hard time calculating $\sin \alpha'$ in a random field, since \hat{b}' in each point is not defined. Instead they use the averaged value on a sphere $\langle \sin \alpha' \rangle = \pi/4$, which is independent on the location on the EATS. We assume a uniform field at each cell with a random direction, thus the code can calculate the actual value of $\sin \alpha'$ at each point. To compare the angular dependency of the simulation output with the 1D analytic expression we divide the intensity at each cell by $(\sin \alpha')^{1-\kappa}$, where κ is the local spectral index (see eq. 15) and average the result over the $\hat{\phi}'$ direction. Figure B1 shows 1D curves of the surface brightness as a function of R_{\perp} (eq. A3). We show curves for

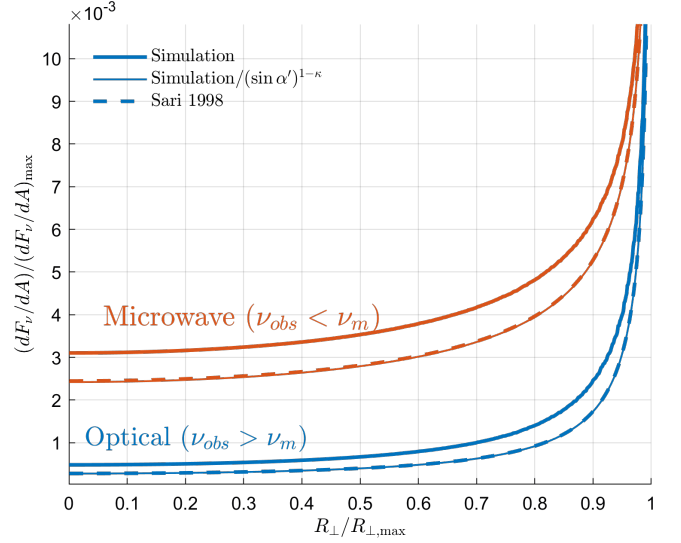


Figure B1. Normalized surface brightness as function of R_{\perp} for two different observed frequencies - optical (blue lines, $\nu_{\text{obs}} > \nu_m$) and microwave (red lines, $\nu_{\text{obs}} < \nu_m$). The results of our simulations at $q = 0$ are shown in solid lines while the analytic expressions of Sari (1998) are in dashed lines.

the optical (blue) and microwave (red) frequencies. Note that we only show the curves from the front of the EATS ($\theta < \theta_{\text{EATS}}$). The dashed lines show the analytic curves. The thin solid lines are the simulation output divided by $(\sin \alpha')^{1-\kappa}$ and the thick solid lines are the full simulation data. All curves are normalised by their maximal value on θ_{EATS} . The thin lines match the analytic results completely. When accounting for the contribution of $\sin \alpha'$, the slope of the curve becomes flatter and as a result the center of the image becomes brighter with respect to the emission at θ_{EATS} . The reason for that is that the average value of $\langle \sin \alpha' \rangle$ decreases with θ . On the LOS $\hat{b}' \perp \hat{\theta}'$ and $\sin \alpha' = 1$, while on θ_{EATS} \hat{b}' can have an arbitrary direction and $\langle \sin \alpha' \rangle = \pi/4$. This effect is not captured by the analytic formula. In addition we can see the effect of the spectral slope on the curves, where the radio image is less limb brightened than the optical image.

Next, we test the time evolution of the integrated flux in our code by comparing the lightcurve in the optical band to the analytic model of Sari et al. (1998). The authors calculated the flux coming from a spherical shock, not accounting for photon arrival time effects and approximating the Doppler factor as a step function where $D = \Gamma$ for $\theta < 1/\Gamma$ and 0 elsewhere. To make a proper comparison we ran a limited version of the simulation with a spherical shock and without photon arrival times. The two lightcurves are presented in fig. B2. The analytic curve is shown in dotted blue line and the result from the limited run in a dashed blue line. To match the results we multiply the analytic curve by a factor of 8, which originates from two effects: i) The exact integral of the Doppler factor over the spherical shock is 4 times larger than the integral of the step function. ii) another factor of 2 comes from differences in the constants used by Sari et al. (1998) when calculating the emission power, with respect to Rybicki & Lightman (1979). To demonstrate the effect of the photon arrival time we add a plot from the full simulation (solid blue line). The peak of the lightcurve occurs at a later time, since the emission comes from a ring of matter with a larger Lorentz factor than on the LOS, thus the observed frequency in the proper frame is smaller and is crossed by ν_m at a later time.

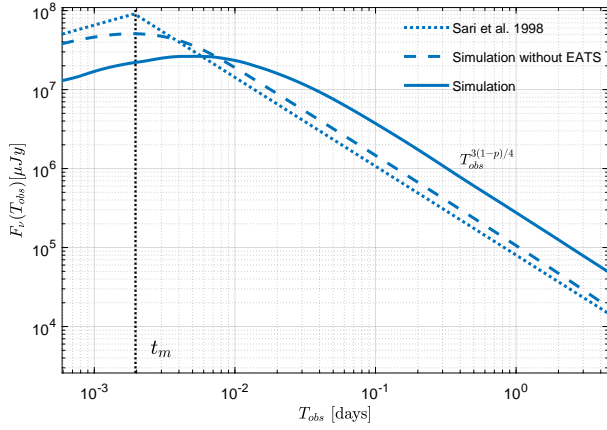


Figure B2. A comparison of optical light curves from a spherical AG shock (no jet break) with a slow cooling emission. We present the analytic calculation from [Sari et al. \(1998\)](#), dotted line) together with a simulated light curves without accounting for light travel times (dashed line) and when accounting for it (solid line). The analytic light curve is multiplied by 8 to match the simulated curve. See the text for an explanation on the origin of the factor.

This paper has been typeset from a \LaTeX file prepared by the author.